



Mapping the geological fault zone that triggered the Mw 6.1 Pasaman earthquake in Indonesia on the basis of gravity anomalies

Muhammad Yanis^{1,2*}, Riski Ananda³, Muhammad Ridha Adhari¹, Andri Yadi Paembonan⁴, Azman Abdul Ghani⁵

¹Geophysical Engineering Department, Universitas Syiah Kuala, Banda Aceh 23111, Indonesia ²Tsunami and Disaster Mitigation Research Center (TDMRC), Universitas Syiah Kuala, Banda Aceh 23111, Indonesia ³Geophysical Engineering Department, Faculty of Mining and Petroleum, Bandung Institute of Technology, Bandung 40132, Indonesia

⁴Geophysical Engineering Department, Sumatera Institute of Technology, Lampung 35365, Indonesia
⁵Department of Geology, Faculty of Science, University of Malaya, 50603 Kuala Lumpur, Federal Territory Malaysia
*corresponding author, e-mail: yanis@usk.ac.id

Abstract

Indonesia's Great Sumatran Fault (GSF) is well known for its destructive capability, having generated many moderate to strong earthquakes, causing damage. A better understanding of GSF characteristics is needed to mitigate future geological hazards in Sumatra and prevent unnecessary loss and damages. The present research aims to map the fault structure in West Pasaman, Indonesia, using the Topex satellite and global gravity model plus (GGM+). Residual anomalies from Bouguer data (50–80 mGal) show a continuous pattern between the confluence of the Angkola, Sumpur and Sianok fault segments in the Pasaman. The vertical and horizontal derivatives were also applied in order to clarify fault structure, which is demonstrated by high derivative anomalies (0.05–0.08 mGal/m) in the horizontal and 0.1 mGal/m in the vertical. Moreover, a cross sectional model from the 3D algorithm (Occam and Singular Value Decomposition) may show the presence of several segments/faults in the Pasaman region, such as the Angkola, Barumun and Sumpur faults with high-density values of $\rho = 2.3-2.4$ g/cm³. Based on results obtained, the use of Topex and GGM+ has provided an overview of the effectiveness of global gravity in mapping faults in the Pasaman region. It is a time-consuming, yet inexpensive method that can be applied to other areas, especially those that are difficult to reach.

Keywords: Gravity satellite, GGM+, Topex, Great Sumatran Fault, Pasaman region

1. Introduction

Sumatra Island (Indonesia) is located at the confluence of two plates, namely the Eurasian Plate and the Indo-Australian Plate, which form a subduction zone (McCaffrey, 2009). Geologically speaking, Sumatra Island is also associated with the Great Sumatran Fault (GSF) system, extending over about 1,900 km from Lampung to India's Andaman Islands. The

active subduction zone triggers the GSF, forming 19 fault segments and 13 separate basins along the structures (Dewanto et al., 2022). The Sumatra one, situated in a subduction zone, causes the region to be very vulnerable to tsunamis and earthquakes that may generate very destructive hazards and tectonic movement activation along the GSF, causing the Sumatra region to be frequently hit by destructive earthquakes (Wirth et al., 2022). On February 25,

2022, the West Pasaman area and its surroundings were impacted by an earthquake with a magnitude of Mw 6.1. This earthquake occurred after a Mw 6.6 earthquake struck West Java in January 2022. The United States Geological Survey (USGS) also reported that the earthquake led to 19 fatalities, 425 injured and four missing people, as well as 4,831 houses and 125 public buildings damaged. It also triggered landslides in West Sumatra, where the Indonesian Agency for Meteorological, Climatological and Geophysics (BMKG) indicated that the epicentre of the Pasaman earthquake was at a depth of about 10 km (Dewanto et al., 2022). The events followed the general main shock-aftershock sequence. The topographic map of the research area, based on the 30 m/px Shuttle Radar Topography Mission (SRTM) data, also contains the main shock and aftershock data from the Pasaman earthquake (Fig. 1).

The main shock of the earthquake examined occurred in the shallow crust along the southern segment of the Angkola Fault, i.e. an active fault that crosses Sumatra Island lengthwise. An analysis conducted by BMKG showed that the foreshock and main shock resulted from a strike-slip motion along the right-lateral fault, which is consistent with the known movement of the GSF. In view of the fact that the earthquake occurred on land, it did not have the

potential to cause a tsunami. However, disaster mitigation is needed to reduce casualties and damage, and earthquake characteristics need to be studied. Several studies have been conducted into the Pasaman area, but these have focused only on efforts to heal trauma to victims and carry out post-earthquake surveys (Kardo et al., 2022). There has yet to be a study of the area's characteristics of faults and earthquakes. Therefore, the present study applies a geophysical method using global gravity data, i.e. Topex and Global Gravity Model Plus (GGM+) data to identify fault structures that can cause earthquakes. The data have been successfully used in several studies, such as fault mapping at the Geuredong volcano (Yanis et al., 2021), analysis of liquefaction potential in central Sulawesi (Fauzik et al., 2020), identification of earthquake source parameters (Lewerissa et al., 2021), mapping of subsurface structure of the Al-Ain region, Emirate of Abu Dhabi (Saibi et al., 2019), East Antarctic tectonic mapping (Riedel et al., 2012) and investigation of structural continuity of the central Japan Fault (Wada et al., 2017).

Fault mapping is generally conducted using seismological studies requiring field instruments (Weller et al., 2012; Muksin et al., 2019; Tiwari & Paudyal, 2022). In contrast, gravity surveys over a large area such as the Pasaman region will require

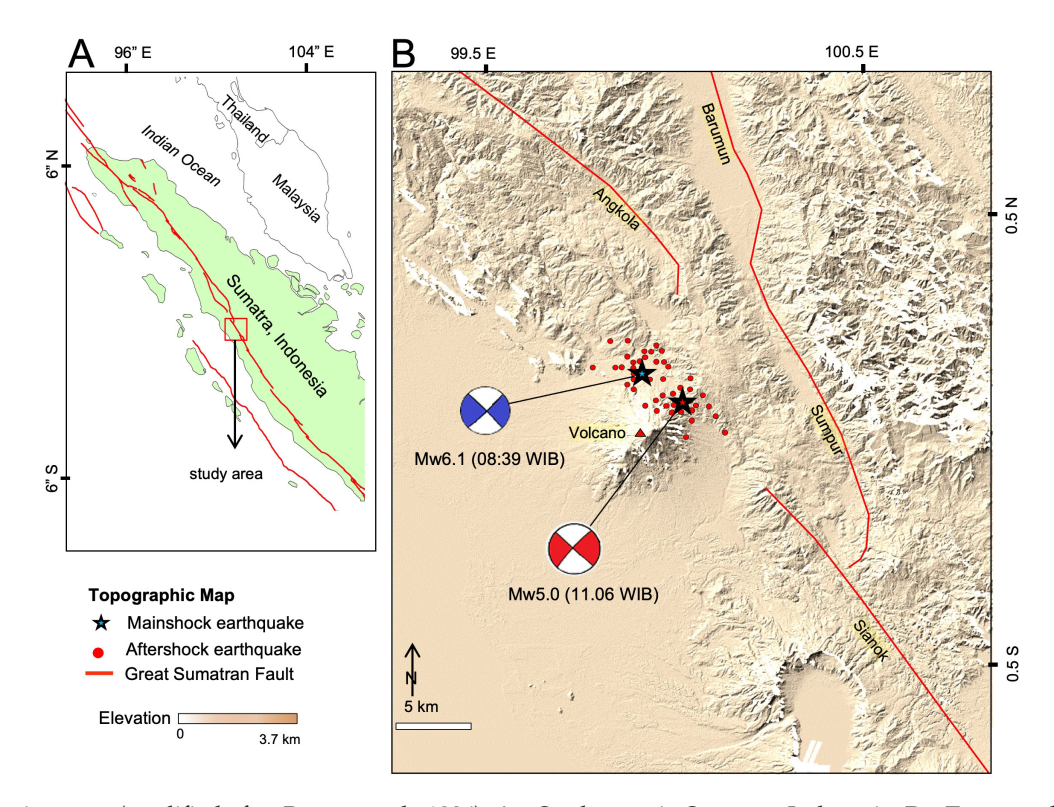


Fig 1. Location map (modified after Bennet et al., 1996). **A** – Study area in Sumatra, Indonesia; **B** – Topographical map of 30 m/px from SRTM data showing several main shocks and aftershocks of the Pasaman earthquake. WIB – West Indonesian Time, when the earthquake occurred.

a lot of time and financial resources, thus making global gravity data a possible solution (Yanis et al., 2021). Earthquake mapping in the Pasaman area has been conducted using seismicity analysis (Wulandari & Chan, 2022), as well as global gravity, which is only limited to analysing the distribution of Bouguer anomalies above the surface (Dewanto et al., 2022). However, 3D gravity modelling may provide information on fault structure and depth in the Pasaman region.

The present study aims to identify the fault structures based on vertical, horizontal and 3D inversion from the Topex and GGM+ data. Research of lateral rock density differences at various depths was also associated with fault structures. Gravity satellite data currently constitute an interesting way to study the presence of faults and geological objects in the subsurface (Gruber et al., 2011; Rexer & Hirt, 2015; Yanis et al., 2023).

2. Geological and tectonic setting

Tectonically, the Sumatra region is strongly influenced by the convergence of the Indo-Australian and Eurasian plates, which forms a subduction zone and moves obliquely at a speed of about 5-6 cm/year to the north (Mosher et al., 2008; Meltzner et al., 2015). It also creates the GSF that stretches over 1,900 km from Lampung to the Andaman Sea (India). Along this fault, there has been a considerable history of seismicity, especially in the southern part of Sumatra (Sieh & Natawidjaja, 2000). The most recent significant seismic activity in the north was noted 170 years ago. Sumatra Island is characterised by a tectonic system divided into three parts: the oblique subduction zone, the Mentawai Fault and the GSF. The oblique subduction zone has a gentle subduction angle stretching from north Sumatra to the province of Lampung. This causes frequent tectonic earthquakes in the western region of Sumatra (Genrich et al., 2000; Hill et al., 2015).

The Mentawai Fault is a strike-slip fault that is parallel to the GSF, located between the subduction zone and the GSF (Diament et al., 1992). The GSF is a strike-slip fault in an area with very high seismic activity, consisting of at least 19 segments (Sieh & Natawidjaja, 2000). Frequent earthquakes in the fault area, including the Pasaman earthquake with a magnitude of Mw 6.1 on 25 February 2022, have

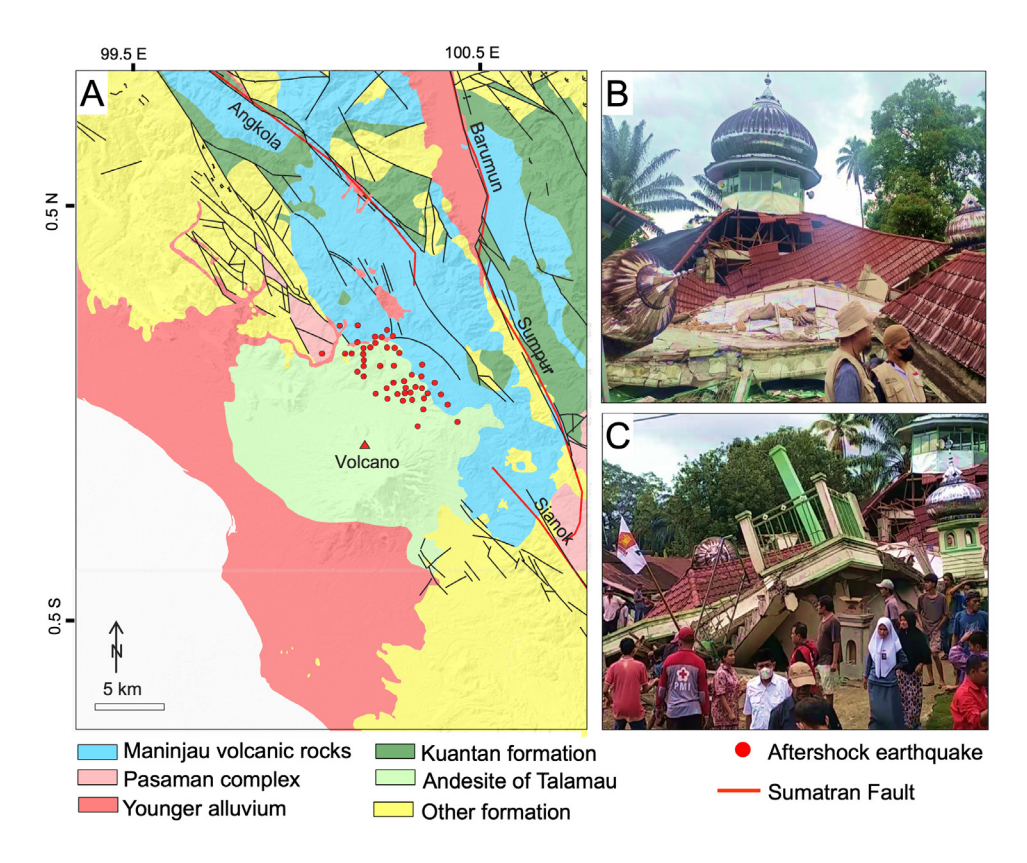


Fig. 2. Geology and effects of the earthquake studied. **A** – Geological map depicting rock/sediment formations in the Pasaman earthquake area; **B**, **C** – Examples of damage to public facilities due to the 6.1 magnitude earthquake on February 25, 2022 (from sumbarkita.id and republika.id).

led to damage to many buildings and the loss of many lives (Fig. 2). In addition, prior to the Pasaman earthquake, most of the seismic activity was detected in the Angkola and Sianok segments of the GSF (see Figs. 1B, 2A; Wulandari & Chan, 2022).

The geological map shows that, in general, the West Pasaman region is covered by Quaternary deposits of the Talamau volcano (Fig. 2A). They comprise lava, tuff and alluvium streams, which have experienced weathering. Most of these rocks are easily detached, soft, decomposed and unconsolidated; hence, they will be vulnerable to shocks when an earthquake occurs. The younger alluvium is located southwest of the fault zone, while the andesite of Talamau is in the volcano region. The younger alluvium in Sumatra refers to relatively recent sediments, composed mainly of sand, silt and clay, as transported and deposited by rivers and mass movements. All these sediments, which result from the island's tectonic activity that leads to frequent earthquakes and volcanism, are of Quaternary age, i.e. younger than 2.6 Ma (Julius et al.,

The sediments contain essential information on the island's geological history, including its tectonic activity, climate and environmental changes (Dewanto et al., 2022). Thus, scientists can investigate the composition and properties of sediments to learn more about the past and present geological processes on the island. For example, andesite of Talamau (Fig. 2A) is an intermediate volcanic rock typically composed of plagioclase feldspar, pyroxene and hornblende. It is characterised by a porphyritic texture, which means that it contains large crystals of minerals (phenocrysts) within a more finely grained matrix. It provides important information on the island's volcanic history, inclusive of the study area (Barber et al., 2005).

3. Material and methods

3.1. Basic theory and data processing

Gravity surveys may be conducted through ground surveys, airborne surveys, shipborne surveys and satellites. Although the ground survey of gravity data has a high degree of accuracy, it is challenging to conduct in remote areas and thus limited to regional studies. Therefore, it could be done with the shipborne and airborne surveys. Unfortunately, both surveys are more costly. Hence, satellite data may be an alternative for providing global gravity data.

3.2.Data set of global gravity

Currently, global gravity data are available at various resolutions. This type of data has a much lower resolution than field measurements, e.g. Earth Gravity Model 2008 (EGM2008) being one of the global gravity data that provide free-air anomalies and Bouguer anomalies with a grid resolution of around 2.5 arc-minutes or 4,625 km per grid data (Pavlis et al., 2012). In addition, there are also Grace Satellites (Gravity Recovery and Climate Experiment) and GOCE (Gravity Field and Steady-State Ocean Circulation Explorer), which provide changes in the Earth's gravitational field data. Using these data, Hirt et al. (2013) developed a high-resolution global gravity model, i.e. Global Gravity Model Plus (GGM+). However, subsurface geological information from data is distributed only at a scale of 10 km. This is because the high resolution of data is merely a topography feature and does not correlate with the distribution of subsurface anomalies.

The GGM+ provides five data types: gravity disturbance, acceleration, north-south deflection, eastwest deflection and quasi-geoid height. These data have been used to study the fracture structure in the Andaman Subduction Zone (Rao et al., 2011), the fault causing earthquakes in Chile, and to identify the liquidation potential in central Sulawesi (Fauzik et al., 2020). In addition, Topex provides the topography data on the surface of the earth and anomalies of gravitational fields in a grid of 1 arc-minute resolution equivalent to 1.85 km/px. Thus, free-air anomaly data from Topex and GGM+were compared in the study area (Fig. 3).

In the present study, two different resolutions of satellite gravity were used to provide better interpretations than ground-based measurements, which did not validate the results obtained. In addition, 3D density inversion can only be done with Topex data, but GGM+ may provide information on the presence of faults based on Bouguer anomalies. Thus, a combination of these two global gravity measurements may properly map the presence of faults in the Pasaman area. Anomaly from Topex data shows a smoother contour than GGM+ because the Topex resolution is lower. This is in contrast to the free-air anomaly from GGM+, which offers a very detailed contour. The free-air anomalies from Topex, which offer a more regional anomalous response, are easier to use in studies of large areas. The identification of regional structures (Fig. 3A), and the free-air anomaly from GGM+ show very good details. However, it most likely contains many topographic details (Fig. 3B). As far as published literature sources are concerned, the

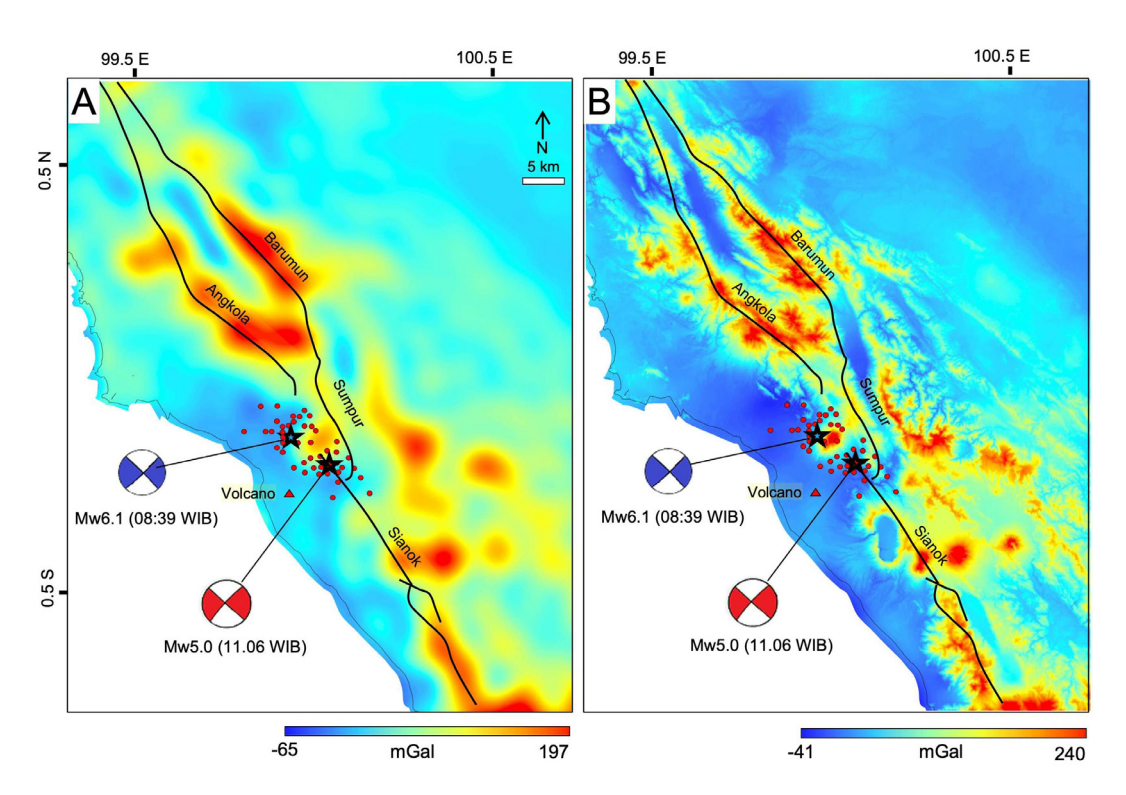


Fig. 3. Free-air anomaly from global gravity data. **A** – Topex data with a resolution of 1.85 km/px; **B** – GGM+ with a high resolution of 200 m/px overlain by faults and distribution of seismic activity from the Pasaman earthquake. For explanations see Figure 1.

Topex satellite has been used in many cases, such as for analysis of the fault structure in the Geureudong volcano area (Yanis et al., 2022b), and study of displacement characteristics of the Anatolian Fault using gravity and GPS data (Pamukçu et al., 2015).

Global gravity data have been successfully used to examine the existence of faults and geological structures below surface (van der Meijde et al., 2015). Mapping for large areas does not require comparison to field measurements because the resolution of satellite data such as GGM+ and Topex is considered effective for describing fault anomalies below the surface. In several cases, it has been demonstrated that the gravity distribution at ground stations has a lower resolution than satellite data (Nasuti et al., 2012; Lenhart et al., 2019). According to Vaish and Pal (2015) and Yanis et al. (2021, 2022b), satellite gravity has the same pattern as CG5 Autograv data, which is standard equipment in ground gravity surveys, and is also similar to the response of shipborne gravity. Therefore, although satellite data are not validated by ground measurement; yet, but for regional surveys such as the Pasaman region, the data can be used as a lowcost and fast preliminary method for mapping the subsurface fault structure. This technique has also been used in other regions of the world regions for mapping faults using gravity satellites.

3.3. Data correction

In order to obtain the full Bouguer anomaly, unlike ground gravity data, several corrections are called for. Satellite data require only two corrections, namely Bouguer and terrain ones. Data obtained from Topex and GGM+ satellites are in the form of gravity disturbance or free-air anomalies. The difference in gravity acceleration to elevation in the surface, with terrain correction to reach the complete Bouguer anomaly, was performed by Hummer Chart (Yanis et al., 2017, 2022a). In this case, the SRTM data with 30 m/px were used as elevation data in the study area. Mathematically, the Bouguer data from satellite gravity may be calculated using eq. 1.

$$\delta g_{\scriptscriptstyle R} = 2\pi G \rho h = 0.4193 \ \rho h \tag{1}$$

where ρ is a rock density used for 2.67 g/cm³ as representing average rock density in the study area, h is height difference between two stations, and G is the gravitational constant = 6.67384×10^{-11} m³ kg $^{-1}$ s $^{-2}$. A spectrum analysis approach can separate residual anomalies from Bouguer anomalies by transforming spatial domain into frequency or wave numbers through 2D Fourier transformation, as shown in eq. 2.

$$\Delta G(k_{x'}, k_{y}) = \int_{-\infty}^{\infty} \int_{-\infty}^{\infty} \Delta g(x, y) e^{-i(k_{x}x + k_{y}y)} dxdy \tag{2}$$

where $\Delta G(k_x, k_y)$ is an anomaly of gravity in the domain of wave numbers and $\Delta g(x, y)$ is an anomaly of gravity in the directions x and y, while a power spectrum graph of $\Delta G(k_x, k_y)$ is obtained for wave number k_x and k_y . The graph shows a straight-line equation that can distinguish the distribution of regional anomalies, residuals and even noise. To obtain residual anomalies, the cut-off of wave numbers between regional and residual anomalies is used as a cut-off wave length in high-pass filtering.

3.4. Derivative filtering

Bouguer anomaly results from accumulation of anomalous mass in the subsurface. This makes it possible to determine the boundaries of the anomaly in the form of geological boundaries and fault structures with data enhancement techniques (Pham et al., 2020). There are many such techniques for increasing the anomaly boundary resolution, including horizontal derivative (Ferreira et al., 2013; Ghosh, 2019), vertical derivative (Gönenç, 2014; Vaish & Pal, 2015) and tilt derivative (Oruç, 2011; Doğru et al., 2017), as well as several developments of previous techniques (Cooper, 2020; Thanh Pham et al., 2021). In the present study, the horizontal derivative method was applied to map the geological boundaries and fault structures of the Bouguer anomaly data. This technique reveals geological boundaries based on the maximum value of subsurface anomaly sources (Thanh et al., 2019). Horizontal derivatives are obtained by calculating the anomaly gradient in the direction of and y, as shown by eq. 3 following:

$$HD = \sqrt{\left(\frac{\partial \Delta g}{\partial x}\right)^2 + \left(\frac{\partial \Delta g}{\partial y}\right)^2} \tag{3}$$

However, some small sources of anomalies near the surface responded to a weak gradient amplitude compared to a large, deep anomaly (Gönenç, 2014). Therefore, vertical derivative (VD) techniques can be applied to map the boundaries of shallow anomalies well, mathematically obtained by eq. 4.

$$VD = \frac{\partial^2 \Delta g}{\partial z^2} = -\left(\frac{\partial^2 \Delta g}{\partial x^2} + \frac{\partial^2 \Delta g}{\partial y^2}\right)$$
(4)

The VD represents the gradient change rates from gravitational anomalies. In turn, the first de-

rivative form is a gradient of gravitational anomalies, which is processed using Potensoft MATLAB (Özgü Arisoy & Dikmen, 2011).

3.5. 3D inversion of Bouguer anomaly

The subsurface density model is calculated on the basis of the residual anomaly of Topex data through inversion modelling. The Grablox 1.6 is used to obtain density anomalies from the subsurface. The algorithm of this code combines two inversion methods, namely Singular Value Decomposition (SVD) and Occam inversion, which are processed simultaneously to arrive at a density model that matches the subsurface rocks (Pirttijarvi, 2014). This method is also often applied to electromagnetic inversions, such as magnetotelluric fields (Marwan et al., 2021) and very low-frequency fields (Yanis et al., 2017, 2022a). Mathematically, the density parameter and depth are obtained by eq.5.

$$\Delta g(r) = g_z(r) = G \frac{\partial}{\partial_z} \int_v \frac{\rho(r')}{|r - r'|} dV'$$
 (5)

where:

G as a gravity constant, $r = (x-x_0)i + (y-y_0)j + (z-z_0)k$ provide the vector position of data measuring, r' as a vector in the integration of volume V, and $\rho(r')$ is the material density at the location r'.

In the present research, the Occam algorithm is applied to solve nonlinear geophysical problems which is a modification of the Levenberg-Marquardt inversion. Compared to the Least Squares inversion, the Levenberg-Marquardt inversion is more effective. It has a more rapid calculation time because it runs in two circumstances at once when the misfit is too small or too large. In the Occam inversion, the Levenberg-Marquardt inversion algorithm is modified by adding α parameters such as a smoothing factor and Tikhonov regulation (L) first order. The following equation shows the algorithm used for the Occam inversion (Martakusumah & Srigutomo, 2015).

$$m_{n+1} = [J_n^T J_n = \alpha^2 L^T L]^{-1} J_n \hat{d}$$
 (6)

where

$$\hat{d} = d - g(m_n) + J_n m_n \tag{7}$$

 m_n is a model parameter in the form of density, J_n is a Jacobi matrix, d is observation data, namely residual anomaly, and $g(m_n)$ a kernel function to the model. In the inversion process, data are arranged

in matrix form. Therefore, the SVD technique is also applied in addition to utilising the inversion algorithm. This is a numerical analysis technique for diagnosing a matrix kernel as a forward modelling function in the inversion process using SVD (Silvennoinen & Kozlovskaya, 2007). The 3D model grid applied to the Pasaman region is presented in Figure 4.

The input data used in the modelling process is a residual anomaly with results in a 3D density model. The final model has an RMS (root mean square) of 0.1 mGal. Besides, the density range used in this inversion process is 2.0–2.4 g/cm³, covering rock contrast from the study area. The Occam algorithm can generate a smoother model than the SVD, so in Grablox software, the model results are combined based on these two algorithms. Mathematically, the RMS error was obtained by compar-

ing calculated data with observations, which can be written as shown by eq. 8 (Pirttijarvi, 2004; Abdel Zaher et al., 2018).

$$RMS_d = \sqrt{\frac{1}{M} \sum_{i=1}^{M} \left(\frac{d_1 - y_1}{\Delta d} \right)^2}$$
 (8)

where Δd is gravity anomaly (d_{max}) a minimum anomaly of gravity observation (d_{min}) using for scaling data. In order to obtain a 3D model, an input matrix was provided with the number of blocks nx = 35, ny = 35, and nz = 10, with a total of 1,225 blocks, where the background density value was set from 2.0–2.4 g/cm³ in response to volcanic rocks. Due to the high ambiguity of 3D gravity, the earthquake epicentre data from USGS/BMKG were used as initial depth solution, which is 30 km (Fig. 4B).

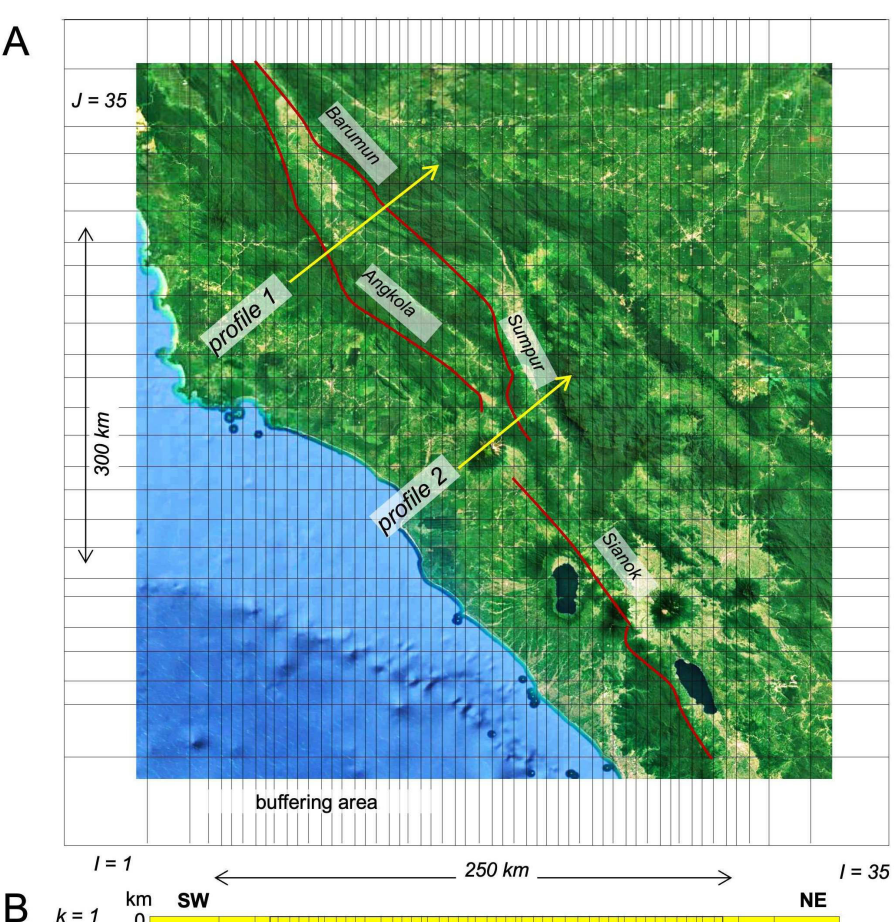


Fig. 4. Resolution of the matrix used in 3D inversion: **A** – Plan view of the grid 3D inversion; the grid in the nx = 250 km and ny = 300 km that covers the Pasaman earthquake region; **B** – Depth slice model; the matrix data at a depth of nz = 30 km, where P1 and P2 are 2D cross-sections extracted from 3D density model.

4. Results and interpretation

GGM+ and Topex gravity data with different resolutions were used to analyse the presence of geological structures, such as faults correlated with the Pasaman earthquake. Various analyses were used to clarify the presence of these faults, such as the separation of regional and local anomalies, derivatives and 3D density (Figs. 5, 6). This technique has been widely applied in global gravity studies for mapping subsurface geological structures.

4.1. Bouguer anomaly

The Bouguer anomaly obtained from Topex data ranges from -125 to 94 mGal (Fig. 5A), from GGM+ data from -56 to 98 mGal (Fig. 5B). These data have a high resolution of 200 metres/pixel that cannot be inversed. This is because these are not original satellite gravity data, but artificial gravity calculated from several data sets (Hirt et al., 2013; Yanis et al., 2021). On the other hand, GGM+ data from remote locations cannot be effectively used to find regional anomalies either. This is because short wave lengths can make it difficult to detect long wave lengths as reflections of regional anomalies.

Therefore, in the present research, only GGM+ data are applied in order to find residual and regional anomalies, derivatives and subsurface density inversion in advanced process steps.

The variation of the Bouguer anomaly is strongly influenced by contrasting rock density and geological structure distribution in the subsurface (Reynolds, 2011). In the present study, the difference between the Bouguer anomaly values from two data sets was due to data resolution needing to differ (Fig. 5). However, the data may describe a similar pattern of anomalies in the region. The high Bouguer anomaly, ≥80 mGal, predominates in the northeastern region, with a mountainous morphology dominated by the Maninjau volcanic and Pasaman formations (compare Figs. 1B, 2A and 5). The southwestern coastal area, covered by young sedimentary rocks of Quaternary age, is characterised by a relatively lower anomaly value of ≤20 mGal. Their presence/location in combination with the geologically confirmed fault structure is useful here. It allows to obtain a spatial image of the fault that controls seismicity in the Pasaman area. Along the GSF segments such as Barumun, Sumpur, Sianok and Angkola, low Bouguer anomaly values are visible concerning neighbouring areas (Fig. 5).

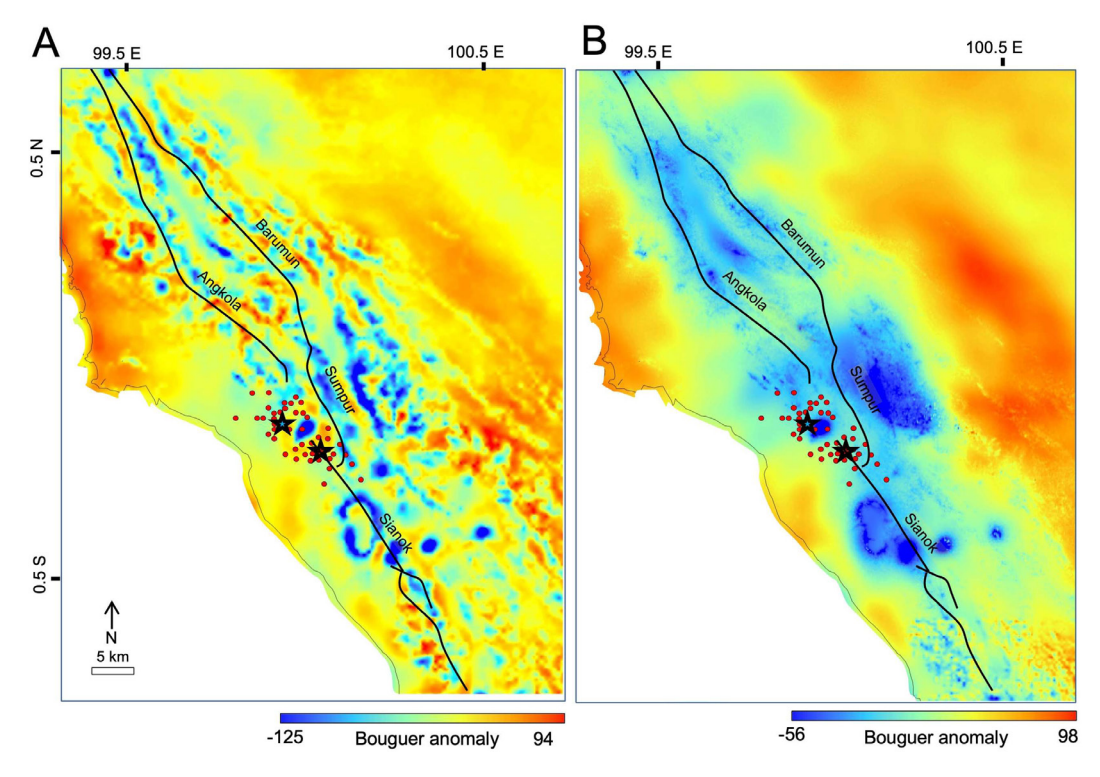


Fig. 5. Bouguer anomaly calculated from a satellite gravity with a density contrast of 2.67 g/cm³; **A** – Topex showing several segments of the GSF; **B** – GGM+ showing the fault area with relatively low values of the Bouguer anomaly. For explanations see Figure 1.

The earthquake epicentre, located in the northeastern part of the Talamau volcano, is indicated by relatively low Bouguer anomalies. This area is controlled by three local segments belonging to the GSF: the Angkola Fault in the north, the Sumpu Fault in the east and the Sianok Fault in the south (Dewanto et al., 2022; Wulandari & Chan, 2022). This allows us to establish a relationship between the active fracture zone and low anomaly values in the Pasaman area. As presented above, GGM+ data can provide more sensitive anomaly contrast than Topex, which allows detection of the presence of even small anomalies in local faults (Fig. 5). However, the Bouguer anomaly does not yet allow us to distinguish between local and regional geological structures (Ribeiro Filho et al., 2018).

4.2. Locale of the Pasaman Fault from residual anomaly

The Bouguer anomaly value combines gravitational effects that are widespread and extend deeply into the observation site. Topex data with a 1.85 km/px resolution were used for advanced data analysis. They allow for a better description of the fault structure than GGM+ data, which contain geological information only on a scale of 10 km. In fur-

ther interpretations, the residual anomaly is needed to obtain a contrast response of rock density that reflects lithological conditions and shallow geological structures (Tong & Guo, 2007; Yanis et al., 2021). Thus, the residual anomalies in the Pasaman area range from –137 to 82 mGal (Fig. 6A).

The residual anomaly value obtained is then superimposed on the geologically identified fault systems. Based on these results, it can be concluded that the fault course is characterised by high and low contrast concerning surrounding areas (Fig. 6A). With regard to areas to the east and west of the GSF, they are characterised by a relatively uniform value of residual anomaly. In the total Bouguer anomaly, a young alluvial lithology is indicated by an anomaly value of about 20 to 40 mGal. When separated by anomalous regional effects of smaller magnitude, it may represent rocks of different densities. Similarly, a residual anomalous andesite body may indicate more clearly the intrusion of the Talamau volcano (compare Figs. 2A and 6).

The residual anomalies also show local structures marked by a high Bouguer value (50–82 mGal), such as on the northern side of the Sumpur and Barumun segments/faults. This is also shown on the southern side of the Angkola and Sianok faults with the same NW-SE direction. These local anomalies can be clearly seen because the residual

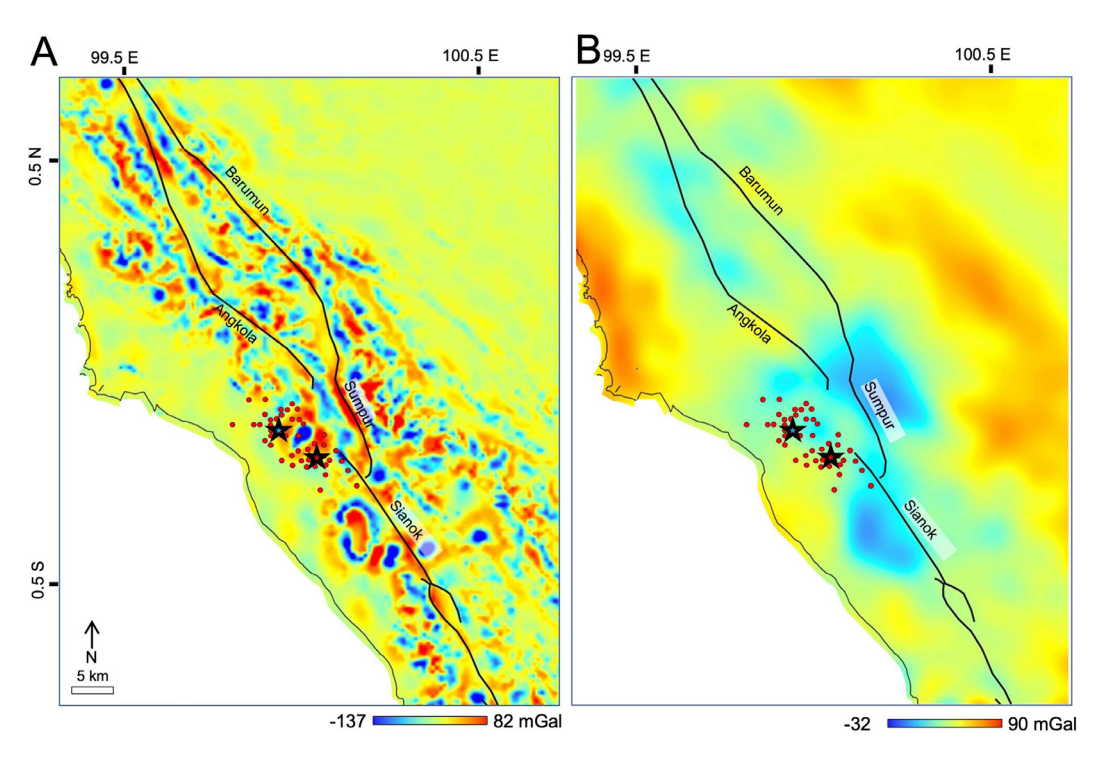


Fig. 6. Residual and regional anomalies in the study area. **A** – Residual anomalies calculated from Bouguer Topex data showing the contrast between the existence of GSF and Mw 6.1 Pasaman earthquake segments; **B** – Regional anomalies showing a general geological contrast. For explanations see Figure 1.

filter removes the long wave length regional anomalies, making the short wave length local anomalies so pronounced (Fig. 6A). On the other hand, regional anomalies generally reflect the state of lithology and do not clearly describe the local geological structure. Their values range from -32 to 90 mGal. The highest regional anomalies (≥70 mGal) occur to the northeast and southwest of the GSF. In comparison, the lowest anomalies (≥10 mGal) are located in the areas of the Talamau volcano, the Sianok Fault and the northern part of the Angkola Fault (Fig. 6B). In contrast to residual anomalies, which can spatially define the boundaries of a fault structure, regional anomalies are not considered capable of providing a detailed description of the subsurface geological structure. Therefore, residual anomaly data are used in the inversion steps.

4.3. Derivative anomaly of the Pasaman Fault

The accuracy of the interpretation and visualisation of geological structures may be improved by using several enhancement techniques so as to clarify the existence of anomalies from gravity data (Fig. 7). Bouguer anomaly data do not allow the determination of faults in several locations where tectonic movements are relatively slower due to deposition or erosion processes (Natawidjaja & Triyoso, 2007). Thus, it is necessary to enhance the data so as to delineate the structures. This approach uses an anomaly derivative to map the boundaries of density changes and the spatial distribution of fault structures beneath the surface (Ferreira et al., 2013). The first filter used is the horizontal derivative (Fig. 7A), which maximises any changes in density in lateral direction below the surface (Cordell & Grauch, 1982; Wada et al., 2017). This filter is considered to minimise noise at the boundaries of internal and shallow structures to help interpret further fault structures (Yanis et al., 2021).

The horizontal derivative anomaly map ranges from 0 to 0.08 mGal/m, where some locations such as the Talamau mountain complex, Talamau volcanic formation and Lake Manunjau boundary, show a high anomaly zone of more than 0.03 mGal/m (Fig.7A). In addition, the horizontal derivative anomalies in local fault zones such as the Barumun, Angkola, Sumpur and Sianok faults also show relatively high anomalous contrast compared to the surrounding area. This may indicate the existence of a regional fault in the GSF segments mentioned. The second filter used is the vertical derivative (Fig. 7B). Despite the weak identified anomaly response, this filter is sensitive to shallow structure response.

It determines fault structures and volcanic manifestations (Yanis et al., 2022b). Vertical derivative values vary between -0.13 to 0.1 mGal/m, where the limit of high and low anomalies dominates the area around the GSF zone. In simple terms, it indicates the presence of geological boundaries and fault structures (Fig. 7B). The anomaly results correspond to the contact response of geological structures in the Pasaman area. There is a continuous pattern between the confluence of the Angkola and Sianok faults, which shows structural discontinuity. Although the main sequence of earthquakes and aftershocks occurred in the GSF system. These events occurred in the above-mentioned gap between the Angkola and Sianok segments. Therefore, it is very important and interesting to learn about the connectivity between the faults to reduce the risk of disasters in the future (Wulandari & Chan, 2022).

The distribution of the Mw 6.1 main earthquake and aftershock in February 2022 could be used as evidence that the fault triggered the quake in the Talamau volcano area, which has long been inactive and not properly mapped (Dewanto et al., 2022). Looking at the pattern of earthquakes occurring, the increase in seismic activity could lead to (a) more severe earthquake(s) in the future. This holds especially true for earthquakes in the Pasaman region, including the GSF system, which is at risk of triggering an even more devastating earthquake (Sieh & Natawidjaja, 2000). The anomaly produced by both techniques shows the same pattern in delineating zones of weakness around the fault area (compare Fig. 7A and 7B). Thus, this is considered effective in validating the geologically predetermined fault distribution. However, the information obtained from the derivative technique is limited merely to distribution above the surface. The inversion technique is carried out to obtain a rock density variation against depth in the subsurface (Lewerissa et al., 2020).

At a location close to the Pasaman earthquake, the horizontal derivative data are similar to the surrounding pattern from the Sumpur and Angkola segments (Fig. 7C). However, at the location of the earthquake with a magnitude of Mw 6.1 that occurred in 2022, the horizontal derivative data allow the location of the fault structure suspected to be the Pasaman Fault. This anomaly is also clearly visible in the vertical derivative data (Fig. 7D). It should be noted that some faults are not reflected in these derivative data either, such as the Sianok segment on the eastern side of the Pasaman area. This may be because the fault is not currently active. Hence, no significant differences in topography and deriv-

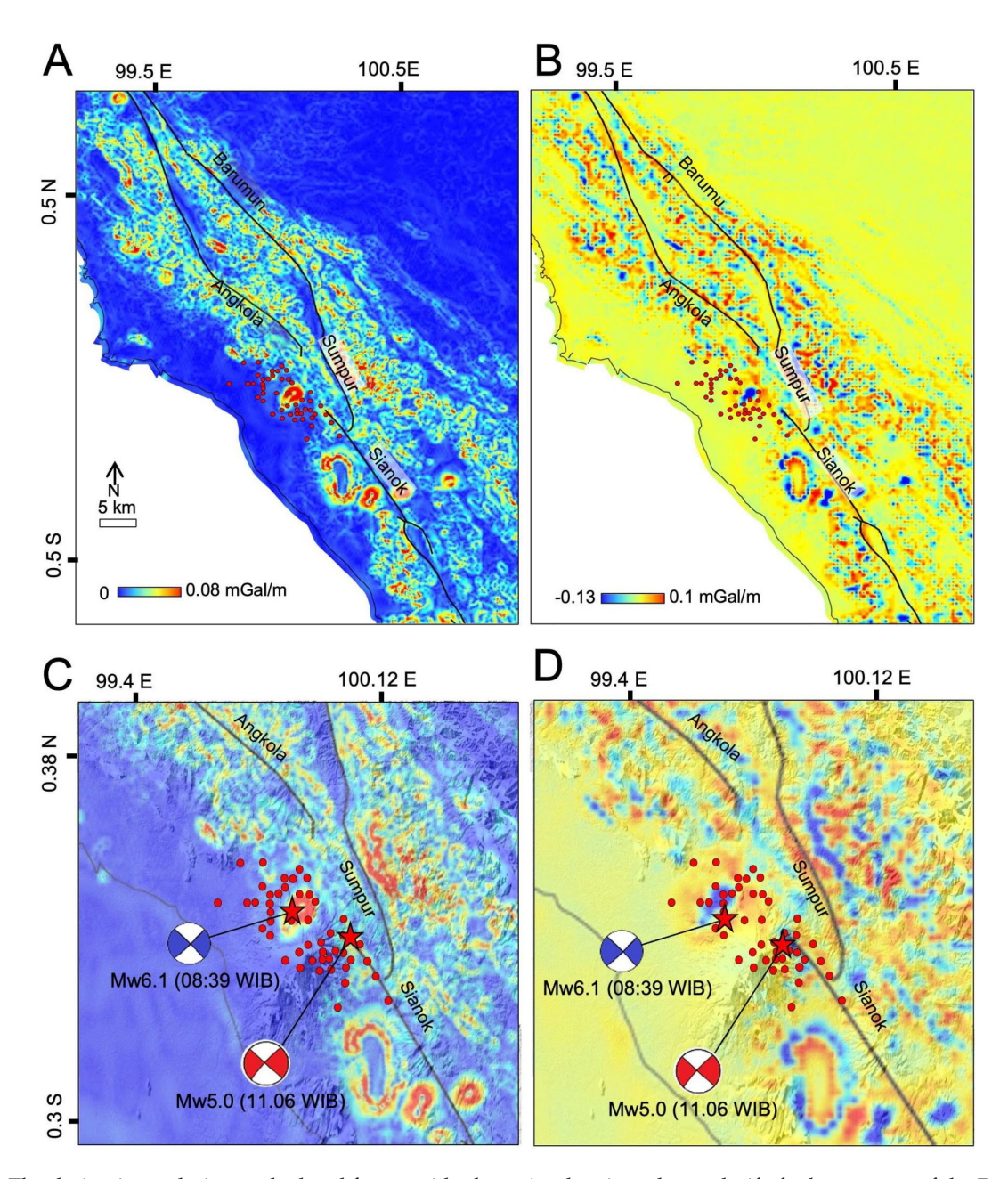


Fig. 7. The derivative technique calculated from residual gravity data in order to clarify fault structure of the Pasaman earthquake; **A** – Horizontal derivative of anomalies; **B** – Vertical derivative of anomalies; **C**, **D** – Derivative anomalies focused on the Pasaman earthquake area only. For explanations see Figure 1.

atives work by detecting variations in terrain elevations on the fault flanks (compare Figs. 1B and 7).

4.4. 3D density of the Pasaman Fault

The density slice is presented here for a depth of 0-20 km and 20-40 km (Fig. 8). As a result, it may be observed that the surface is dominated by low-density rocks in the northern, eastern and northeastern areas (Fig. 8A). In the case of a depth

of 20–40 km, high-density rocks dominate along the fault zone forming the GSF (Fig. 8B). The lineament pattern of the fault structure (i.e. GSF segments) in the first model is generally weakly visible, while in the second model it is relatively more pronounced. In addition, USGS seismicity data demonstrate that the hypocentre of the Pasaman earthquake is located in this weak zone of low-density value, meaning the presence of the Pasaman Fault below the surface (Fig. 8A). In the second slice model, at a depth of 20–40 km, there are high-density rocks located

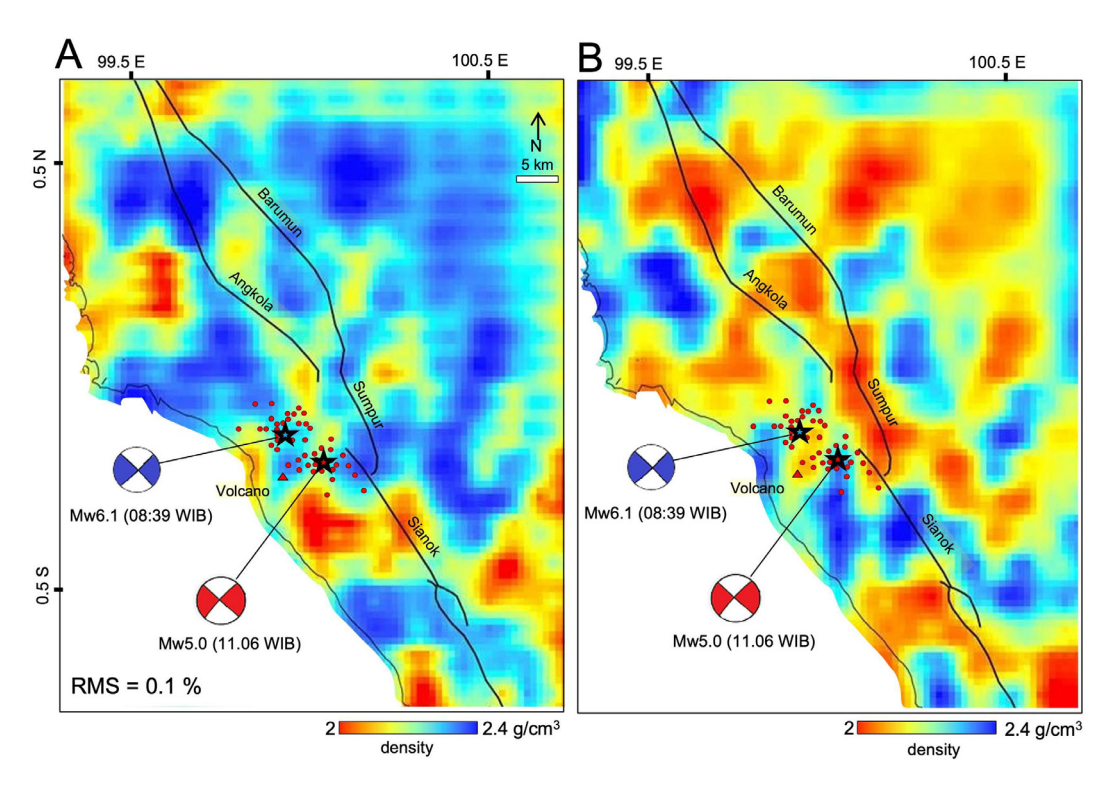


Fig. 8. Density map obtained from 3D inversion in the Pasaman Earthquake area. **A** – Slice density at a depth of 0–20 km; **B** – Slice density at 20–40 km below the surface. For explanations see Figure 1.

below low-density ones in the previous slice model (Fig. 8B). This shows that the deeper you go, the greater the density of rocks due to high pressure and temperature becomes. The nature of the fracture/fault at a depth of 20–40 km is difficult to interpret. It should be noted, however, that the projection of the Pasaman earthquake epicentre point is located at the mentioned depth, i.e. 20–40 km. It may be assumed that this location is very prone to earthquake points.

The cross-section 2D runs for 100 km in a SW-NE direction, crossing the Angkola and Barumun faults. It was extracted from 3D density data to show the location of faults in the Pasaman area (Fig. 9). This cross-section was compared with elevation data from Google Earth and rock formation from the geological map to compensate for the high ambiguity of the gravity inversion. The results obtained show the presence of five different densities in the study area. This is interpreted by the complexity of the underground geological conditions (e.g. structural features, rock formations, etc.) of the Pasaman territory. Near the surface (depth 0-10 km), the density (ρ1) varies between 2.0-2.1 g/cm³, which is most likely related to the volcanic rocks (andesitic and pyroclastic) of the Maninjau mountain. At greater depths the density is higher and amounts to 2.2-2.4 g/cm³ (Fig. 9).

At a depth of 15–30 km, the density value (ρ 2) is recorded to be 2.4 g/cm³, which is interpreted to be related to the scarp of the Angkola Fault. Furthermore, the density value $\rho 3 = 2.3 \text{ g/cm}^3$ is slightly lower, which may also be related to the Angkola Fault. According to the geological map, the area characterised, part of the West Sumatra block, is dominated by the Kuantan Formation (compare Figs. 2A, 4A and 9), which is composed mainly of metamorphic rocks, shales and carbonates. A different density value $\rho 4 = 2.3 \text{ g/cm}^3$ was documented in the more northeasterly part of the cross-section analysed. This density value is interpreted as being related to the scarp of the Barumun Fault, where the area is composed mainly of young alluvial deposits. Finally, the density value was recorded to be $\rho 5 =$ 2.4 g/cm³, which may also be related to the scarp of the same fault in the more northeasterly part composed of the Maninjau volcanic rocks (compare Figs. 2A, 4A and 9). This cross-section (profile 1) shows a density contrast that reflects the geometry of the Angola and Barumun faults in the study area.

Another cross-section (profile 2) was made to intersect the Angola and Sumpur faults in the Pasaman region (compare Figs. 4A and 10). It is 30 km deep, 80 km long and runs in a SW-NE direction. The density value along this profile 1 is in the range of $2.0-2.4 \text{ g/cm}^3$. At a near-surface depth, 0-15 km, the density value is low, i.e., $\rho 1 = 2.0-2.1 \text{ g/cm}^3$, which

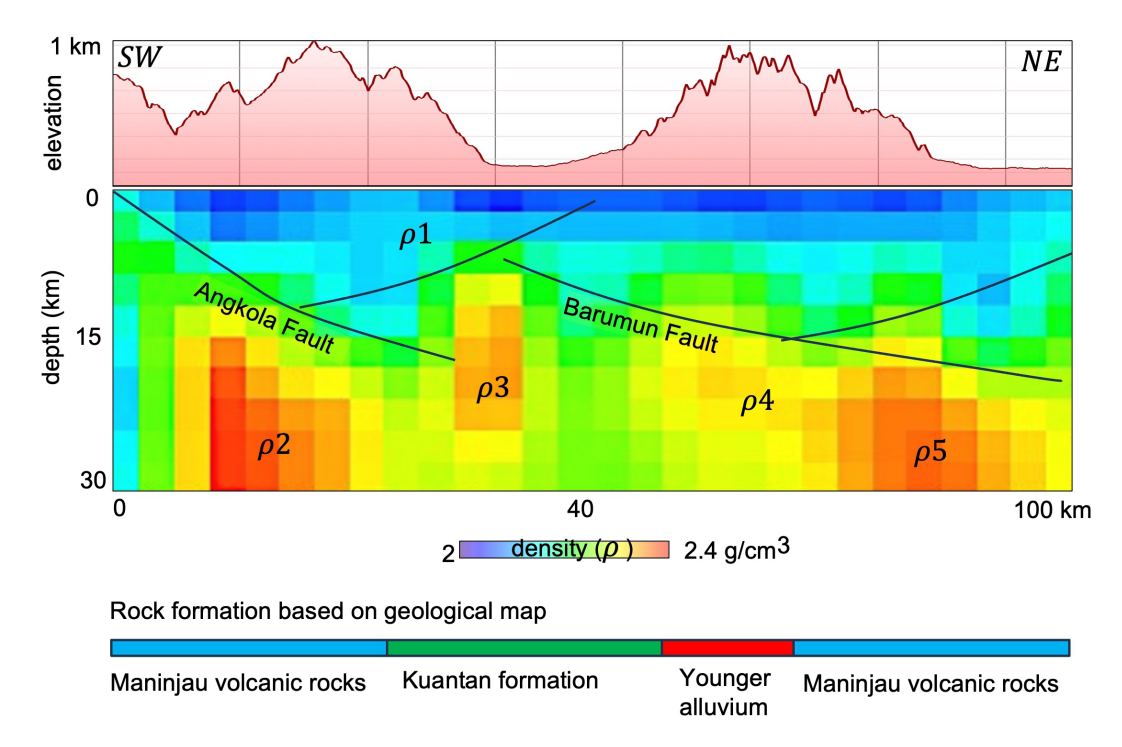


Fig. 9. Cross-section model intersecting the Angkola and Barumun faults – profile 1. The model compares elevations and rock formations from Google Earth and a geological map. For the location of profile 1 see Figure 4A.

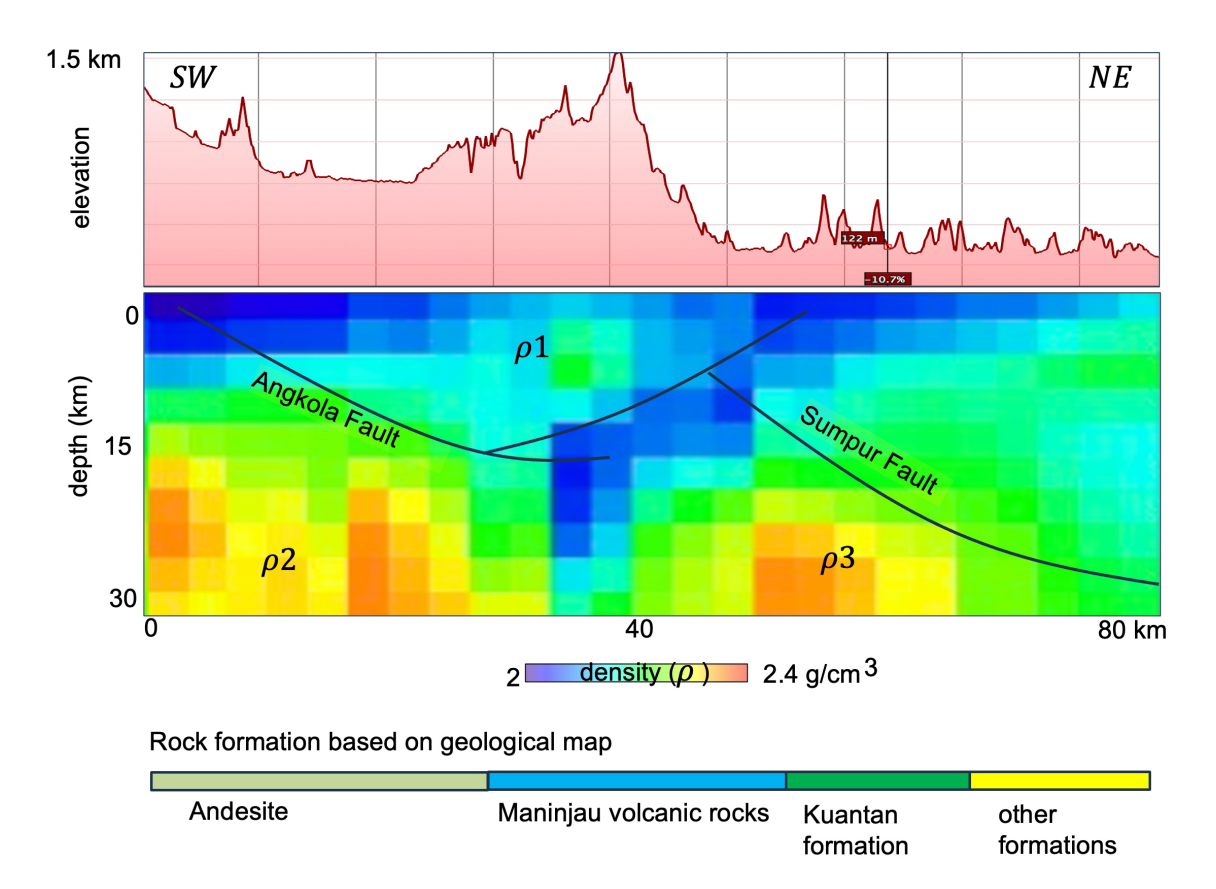


Fig. 10. Cross-section model intersecting the Angkola and Sumpur faults – profile 2. The model compares elevations and rock formations from Google Earth and a geological map. For location of profile 2 see Figure 4A.

may be related to the volcanic rocks (andesites and pyroclastics) of the Maninjau mountain. Meanwhile, at greater depths, 15–30 km, the density value ranges between $\rho 3 = 2.2$ –2.4 g/cm³, which is interpreted as fault systems located in the Pasaman area. The same is true for the density value of $\rho 2 = 2.4$ g/cm³, which is interpreted to be related to the Angkola Fault scarp, and this anomaly is similar to the above-characterised profile 1 (compare Figs. 9 and 10).

In summary, the density value mentioned (ρ 3 = 2.4 g/cm³) is interpreted as related to the Sumpur Fault scarp. This anomaly on the 3D model can also show the contrast between rock formations in the Pasaman area (see Fig. 2A). For example, at a distance of 0–30 km from the start of profile 2 andesites dominate, at a distance of 30-50 km the Maninjau Formation, at a distance of 50-60 km the Kuantan Formation, and at a distance of 70-80 km other rock formations dominate (compare Figs. 2A and 10). Therefore, although gravity inversion is subject to great ambiguity, the results of the present study may still be used for analysing the subsurface geological conditions and characterisng fault systems. The results of the present research were obtained solely from earthquake epicentre data and the geological map of the study area. Hence, further investigations, such as magnetotelluric and tomographic/seismological ones, are necessary to characterise the subsurface condition of the study area better.

5. Conclusions

The Bouguer anomaly obtained from GGM+ and Topex satellite illustrates a similar pattern between the areas with high and low anomalies. This is the case for the eastern regions, which lie behind the Great Sumatran Fault (GSF), where the residual anomaly values are relatively uniform. The regional anomalies in the northeast and southwest of the study area are of high value, while low regional anomalies occur in the Talamau volcano, as well as in the Sianok and northern Angola regions.

The horizontal derivative result shows a zone of high anomaly with a value of up to 0.03 mGal/m at several locations, such as the Talamau mountain, the Talamau volcanic formation and the Lake Manunjau boundary. High contrast anomalies are also visible on local fault routes such as Barumun, Angkola, Sumpur and Sianok. At the same time, the value of the vertical derivative varies from -0.13 to 0.1 mGal along the GSF. The resulting anomalous pattern shows continuity between the confluence of the Angkola and Sianok faults in the Pasaman region. Thus, the 6.1 magnitude Pasaman earthquake

of February 25, 2022, occurred in the gap area between the Angkola and Sianok faults.

The 3D modelling of Topex data was carried out to describe the fault in the West Pasaman region. The density model at different depths indicates inversion of the residual anomaly data at a 40 km depth. In the northeast of the study area, low-density rocks dominate, while in the southeast, high-density rocks are found. The 2D cross-section, obtained from the 3D density model cutting the Angkola, Barumun and Sumpur faults, shows a large density contrast. This is most likely related to the fault geometry in the Pasaman area.

Finally, the density models also illustrate the contrast between rock formations, as confirmed by geological maps. Gravity inversion is known to be highly ambiguous in interpretation. Nevertheless, adding data such as geological information and earthquake epicentres seems purposeful. As a result, the analysis of density contrast caused by different rock formations and faults can help determine the locations of future, devastating earthquakes in the Pasaman region.

Acknowledgements

The authors thank all teams that provided data supporting field results, such as earthquake damage documentation and geological data, as well as the supplier Topex Gravity and are grateful to two anonymous reviewers and the *Geologos* editors, whose constructive comments, suggestions and advice significantly improved the quality of the present paper. This research is part of the 2024 Lektor Research grant funded by Universitas Syiah Kuala under grant No: 344/UN11.2.1/PG.01.03/SPK/PTNBH/2024.

References

Abdel Zaher M., Elbarbary S., Sultan S.A., El-Qady G., Ismail A. & Takla E.M., 2018. Crustal thermal structure of the Farafra oasis, Egypt, based on airborne potential field data. *Geothermics* 75, 220–234.

Barber A.J., Crow M.J. & Milsom J.S., 2005. Sumatra. Geology, Resources and Tectonic Evolution. Geological Society Memoirs 31, London, 290 pp.

Bennet M., Doyle P., Larwood J. & Prosser C., 1996. *Geology on your Doorstep*. The Geological Society, London, 270 pp.

Cooper G.R.J., 2020. A modified enhanced horizontal derivative filter for potential field data. *Exploration Geophysics* 51, 549–554.

Cordell L. & Grauch V.J.S., 1982. Mapping basement magnetisation zones from aeromagnetic data in the San Juan Basin, New Mexico. SEG Technical Program Expanded Abstracts, 246–247.

- Dewanto B.G., Priadi R., Heliani L.S., Natul A.S., Yanis M., Suhendro I. & Julius A.M., 2022. The 2022 Mw 6.1 Pasaman Barat, Indonesia Earthquake, Confirmed the Existence of the Talamau Segment Fault Based on Teleseismic and Satellite Gravity Data. *Quaternary* 5, 45.
- Diament M., Harjono H., Karta K., Deplus C., Dahrin D., Zen Jr M.T., Gerard M., Lassal O., Martin A. & Malod J., 1992. Mentawai fault zone off Sumatra: A new key to the geodynamics of western Indonesia. *Geology* 20, 259–262.
- Doğru F., Pamukçu O. & Özsöz I., 2017. Application of tilt angle method to the Bouguer gravity data of Western Anatolia. *Bulletin of the Mineral Research and Exploration* 155, 213–222.
- Fauzik D., Haris A., Martha A.A. & Riyanto A., 2020. Liquefaction potential identification in the Central Sulawesi using gravity inversion model in the Central Sulawesi, in: *IOP Conference Series: Earth and Environmental Science*, pp. 1–7.
- Ferreira F.J.F., de Souza J., de Barros e Silva Bongiolo A. & de Castro L.G., 2013. Enhancement of the total horizontal gradient of magnetic anomalies using the tilt angle. *Geophysics* 78, J33–J41.
- Genrich J.F., Bock Y., McCaffrey R., Prawirodirdjo L., Stevens C.W., Puntodewo S.S.O., Subarya C. & Wdowinski S., 2000. Distribution of slip at the northern Sumatran fault system. *Journal of Geophysical Research Solid Earth* 105, 28327–28341.
- Ghosh G.K., 2019. Interpretation of gravity anomaly to delineate thrust faults locations at the northeastern part of India and its adjacent areas using source edge detection technique, tilt derivative and Cos (θ) analysis. *Acta Geophysica* 67, 1277–1295.
- Gönenç T., 2014. Investigation of distribution of embedded shallow structures using the first order vertical derivative of gravity data. *Journal Applied Geophysics* 104, 44–57.
- Gruber T., Visser P.N.A.M., Ackermann C. & Hosse M., 2011. Validation of GOCE gravity field models by means of orbit residuals and geoid comparisons. *Journal of Geodesy* 85, 845–860.
- Hill E.M., Yue H., Barbot S., Lay T., Tapponnier P., Hermawan I., Hubbard J., Banerjee P., Feng L., Natawidjaja D. & Sieh K., 2015. The 2012 Mw 8.6 Wharton Basin sequence: A cascade of great earthquakes generated by near-orthogonal, young, oceanic mantle faults. *Journal of Geophysical Research Solid Earth* 120, 3723–3747.
- Hirt C., Claessens S., Fecher T., Kuhn M., Pail R. & Rexer M., 2013. New ultra-high resolution picture of Earth's gravity field. Geophysical Research Letters 40, 4279– 4283.
- Julius A.M., Pribadi S., Saputra A.A., Prayitno B.S., Ahadi S., Hermanto D., Arifin H., Satria L.A. & Zevanya C.S.S., 2022. An On-Site Post-Event Survey of the 2022 Mw 6.1 West Pasaman Sumatera Destructive Earthquake. *Journal of Renewable Energy* 2, 39–49.
- Kardo R., Rahma Mulyani R. & Yulastri W., 2022. Play Therapy as A Trauma Healing Effort In Children Victims of The Earthquake In Nagari Nagari Pasaman.

- Human: Journal of Community and Public Service 1, 90-94.
- Lenhart A., Jackson C.A.-L., Bell R.E., Duffy O.B., Gawthorpe R.L. & Fossen H., 2019. Structural architecture and composition of crystalline basement offshore west Norway. *Lithosphere* 11, 273–293.
- Lewerissa R., Sismanto S., Setiawan A., Pramumijoyo S. & Lapono L., 2020. Integration of gravity and magnetic inversion for geothermal system evaluation in Suli and Tulehu, Ambon, eastern Indonesia. *Arabian Journal of Geosciences* 13, 726.
- Lewerissa R., Alzair N. & Lapono L., 2021. Identification of Ransiki fault segment in South Manokwari Regency, West Papua Province, Indonesia based on analysis of a high-resolution of global gravity field: Implications on the Earthquake Source Parameters. *IOP Conference Series Earth Environmental Science* 873, 012048.
- Martakusumah R. & Srigutomo W., 2015. Comparison of 1D magnetotelluric inversion using Levenberg-Marquardt and Occam's inversion schemes. *AIP Conference Proceedings* 1656, 070014.
- Marwan, M., Yanis, M., Nugraha, G. S., Zainal, M., Arahman, N., Idroes, R., Dharma, D. B., Saputra, D., & Gunawan, P., 2021. Mapping of Fault and Hydrothermal System beneath the Seulawah Volcano Inferred from a Magnetotellurics Structure. *Energies* 14, 6091.
- McCaffrey R., 2009. The tectonic framework of the sumatran subduction zone. *Annual Review of Earth and Planetary Sciences* 37, 345–366.
- Meltzner A.J., Sieh K., Chiang H.W., Wu C.C., Tsang L.L.H., Shen C.C., Hill, E.M., Suwargadi B.W., Natawidjaja D.H., Philibosian B. & Briggs R.W., 2015. Time-varying interseismic strain rates and similar seismic ruptures on the Nias-Simeulue patch of the Sunda megathrust. *Quaternary Science Reviews* 122, 258–281.
- Mosher D.C., Austin J.A., Fisher D. & Gulick S.P.S., 2008. Deformation of the northern Sumatra accretionary prism from high-resolution seismic reflection profiles and ROV observations. *Marine Geology* 252, 89–99.
- Muksin U., Bauer K., Muzli M., Ryberg T., Nurdin I., Masturiyono M. & Weber M., 2019. AcehSeis project provides insights into the detailed seismicity distribution and relation to fault structures in Central Aceh, Northern Sumatra. *Journal Asian Earth Science* 171, 20–27.
- Nasuti A., Pascal C. & Ebbing J., 2012. Onshore–offshore potential field analysis of the Møre–Trøndelag Fault Complex and adjacent structures of Mid Norway. *Tectonophysics* 518–521, 17–28.
- Natawidjaja D.H. & Triyoso W., 2007. The Sumatran Fault Zone from Source to Hazard. *Journal of Earth-quake and Tsunami* 1, 21–47.
- Oruç B., 2011. Edge detection and depth estimation using a tilt angle map from gravity gradient data of the Kozaklı-central Anatolia region, Turkey. *Pure Applied Geophysics* 168, 1769–1780.
- Özgü Arisoy M. & Dikmen Ü., 2011. Potensoft: MAT-LAB-based software for potential field data processing, modeling and mapping. Computer Geoscience 37, 935–942.

- Pamukçu O., Gönenç T., Çirmik A. & Kahveci M., 2015. Investigation of the Siğacik Bay's displacement characteristic by using GPS and gravity data in Western Anatolia. *Journal of Asian Earth Sciences* 99, 72–84.
- Pavlis N.K., Holmes S.A., Kenyon S.C. & Factor J.K., 2012. The development and evaluation of the Earth Gravitational Model 2008 (EGM2008). *Journal of Geophysical Research: Solid Earth* 117, 1–38.
- Pham L.T., Van Vu T., Le Thi S. & Trinh P.T., 2020. Enhancement of Potential Field Source Boundaries Using an Improved Logistic Filter. *Pure Applied Geophysics* 177, 5237–5249.
- Pirttijarvi M., 2014. Gravity interpretation and modelling software based on a 3-D block model, User's guide to version 2.1. *Geological Survey of Findland*, 1–63.
- Rao N.P., Rao C.N., Hazarika P., Tiwari V.M., Kumar M.R., Singh A. & Sharkov E. V, 2011. Structure and tectonics of the Andaman subduction zone from modeling of seismological and gravity data. Intech Publisher, Rijeka, Croatia, pp. 249–268.
- Rexer M. & Hirt C., 2015. Spectral analysis of the Earth's topographic potential via 2D-DFT: a new data-based degree variance model to degree 90,000. *Journal of Geodesy* 89, 887–909.
- Reynolds J.M., 2011. *An Introduction to Applied and Environmental Geophysics*. 2nd Edition. JohnWiley & Sons, Ltd., Chichester, UK, 712 pp.
- Ribeiro Filho N., Martins C.M. & Santos R.D.S., 2018. A novel regional-residual separation approach for gravity data through crustal modeling. *Brazilian Jour*nal of Geophysics 36, 491–505.
- Riedel S., Jokat W. & Steinhage D., 2012. Mapping tectonic provinces with airborne gravity and radar data in Dronning Maud Land, East Antarctica. *Geophysical Journal International* 189, 414–427.
- Saibi H., Mogren S., Mukhopadhyay M. & Ibrahim E., 2019. Subsurface imaging of the Harrat Lunayyir 2007–2009 earthquake swarm zone, western Saudi Arabia, using potential field methods. *Journal of Asian Earth Science* 169, 79–92.
- Sieh K. & Natawidjaja D., 2000. Neotectonics of the Sumatran fault, Indonesia. *Journal of Geophysical Resources* 105, 28295–28326.
- Silvennoinen H. & Kozlovskaya E., 2007. 3D structure and physical properties of the Kuhmo Greenstone Belt (eastern Finland): Constraints from gravity modeling and seismic data and implications for the tectonic setting. *Journal of Geodynamics* 43, 358–373.
- Thanh L., Erdinc P. & Thanh O., 2019. Edge enhancement of potential field data using the logistic function and the total horizontal gradient. *Acta Geodaetica et Geophysica* 54, 143–155.
- Thanh Pham L., Anh Nguyen D., Eldosouky A.M., Abdelrahman K., Van Vu T., Al-Otaibi N., Ibrahim E. & Kharbish S., 2021. Subsurface structural mapping from high-resolution gravity data using advanced processing methods. *Journal of King Saud University-Science* 33, 101488.

- Tiwari R.K. & Paudyal H., 2022. Frequency magnitude distribution and spatial correlation dimension of earthquakes in north-east Himalaya and adjacent regions. *Geologos* 28, 115–128.
- Tong L.T. & Guo T.R., 2007. Gravity terrain effect of the seafloor topography in Taiwan. *Terrestrial, Atmospheric and Oceanic Sciences* 18, 699–713.
- Vaish J. & Pal S.K., 2015. Geological mapping of Jharia Coalfield, India using GRACE EGM2008 gravity data: a vertical derivative approach. Geocarto International 30, 388–401.
- Wada S., Sawada A., Hiramatsu Y., Matsumoto N., Okada S., Tanaka T. & Honda R., 2017. Continuity of subsurface fault structure revealed by gravity anomaly: the eastern boundary fault zone of the Niigata plain, central Japan. *Earth, Planets and Space* 69, 1–12.
- Weller O., Lange D., Tilmann F., Natawidjaja D., Rietbrock A., Collings R. & Gregory L., 2012. The structure of the Sumatran Fault revealed by local seismicity. *Geophysical Research Letter* 39, L01306.
- Wirth E.A., Sahakian V.J., Wallace L.M. & Melnick D., 2022. The occurrence and hazards of great subduction zone earthquakes. *Nature Reviews Earth & Environ*ment 3, 125–140.
- Wulandari R. & Chan C., 2022. The 2022 Mw 6.2 Pasaman, Indonesia, earthquake and its implication of seismic hazard in central-west Sumatra. *Geoscience Letters* 10, 25.
- Yanis M., Bakar M. & Ismai N., 2017. The Use of VLF-EM and Electromagnetic Induction Methods for Mapping the Ancient Fort of Kuta Lubok as Tsunami Heritage. 23rd European Meeting of Environmental and Engineering Geophysics. *European Association of Geoscientists & Engineers* 2017, pp. 1–5.
- Yanis M., Abdullah F., Zaini N. & Ismail N., 2021. The northernmost part of the Great Sumatran Fault map and images derived from gravity anomaly. Acta Geophysica 69, 795–807.
- Yanis M., Ismail N. & Abdullah F., 2022a. Shallow Structure Fault and Fracture Mapping in Jaboi Volcano, Indonesia, Using VLF-EM and Electrical Resistivity Methods. Natural Resources Research 31, 335–352.
- Yanis M., Marwan, Idroes R., Zaini N., Paembonan A.Y., Ananda R. & Ghani A., 2022b. A pilot survey for mapping the fault structure around the Geuredong volcano by using high-resolution global gravity. *Acta Geophysica* 70, 2057–2075.
- Yanis M., Simanjuntak A., Abdullah F., Marwan M. & Ghani A., 2023. Application of Seismicity and Gravity Observation-Based Filtering Model for Mapping a Fault Structure in Weh Island, Indonesia. *Iraqi Geological Journal* 56, 260–274.

Manuscript submitted: 9 January 2025 Revision accepted: 28 May 2025